climate

MDPI

Article

# Polar Cyclone Identification from 4D Climate Data in a Knowledge-Driven Visualization System

**Feng Wang [1,2], Wenwen Li [1,*] and Sizhe Wang [1]**

[1] GeoDa Center for Geospatial Analysis and Computation, School of Geographical Sciences and Urban Planning, Arizona State University, Tempe, AZ 85287-5302, USA; fwang80@asu.edu (F.W.); wsizhe@asu.edu (S.W.)

[2] State Key Laboratory of Remote Sensing Science, The Institution of Remote Sensing and Digital Earth, Chinese Academy of Sciences, Beijing 100101, China

* Correspondence: wenwen@asu.edu; Tel.: +1-480-727-5987

Academic Editor: Yang Zhang
Received: 2 July 2016; Accepted: 23 August 2016; Published: 5 September 2016

**Abstract:** Arctic cyclone activity has a significant association with Arctic warming and Arctic ice decline. Cyclones in the North Pole are more complex and less developed than those in tropical regions. Identifying polar cyclones proves to be a task of greater complexity. To tackle this challenge, a new method which utilizes pressure level data and velocity field is proposed to improve the identification accuracy. In addition, the dynamic, simulative cyclone visualized with a 4D (four-dimensional) wind field further validated the identification result. A knowledge-driven system is eventually constructed for visualizing and analyzing an atmospheric phenomenon (cyclone) in the North Pole. The cyclone is simulated with WebGL on in a web environment using particle tracing. To achieve interactive frame rates, the graphics processing unit (GPU) is used to accelerate the process of particle advection. It is concluded with the experimental results that: (1) the cyclone identification accuracy of the proposed method is 95.6% when compared with the NCEP/NCAR (National Centers for Environmental Prediction/National Center for Atmospheric Research) reanalysis data; (2) the integrated knowledge-driven visualization system allows for streaming and rendering of millions of particles with an interactive frame rate to support knowledge discovery in the complex climate system of the Arctic region.

**Keywords:** cyclone identification; North Polar; particle tracing; 4D vector data visualization; GPGPU

## 1. Introduction

The polar regions, especially the Arctic, are critically important to the global climate and they play a vital role in ecosystems as well as the global economy. Because of its importance, government agencies from the eight Arctic countries have been developing national/international strategies to better understand and protect this area. For instance, the US government has stressed the significance of the Arctic region using the slogan "Charting and mapping the Arctic region". The US National Science Foundation has established a Polar Cyberinfrastructure program to take advantage of the advanced cyberinfrastructure technology to support the analysis of the Arctic/Antarctic climate phenomena and their change [1–4]. In recent years, a consensus has been reached by climate scientists that the Arctic climate has exhibited significant changes [5,6]. To pinpoint and trace these variances and changes, research has been focusing on analyzing and evaluating observation data on synoptic activity and atmospheric events occurring in this region with statistical methods [7–10].

The visualization of spatiotemporal wind data is regarded as the most intuitive and fundamental process in cyclone analysis. It not only draws a graphical illustration of discrete wind data to facilitate the understanding of the cyclone but it also contributes to the viewing of cyclone characteristics.

Motivated to provide a robust, multi-dimensional visualization and analysis toolkit for polar scientists exploring and researching the complicated Arctic region, a user-friendly and interactive knowledge-driven visualization system on a web environment is ultimately constructed in our work. The cyclone identification submodule enables scientists to obtain knowledge from raw atmospheric data. The wind simulation submodule, on the other hand, significantly contributes to the validation of knowledge and to eventually solving the challenges of decision-making in North Polar matters.

In the field of scientific data visualization, studies indicate that research topics shift from visualizing small, isolated spatial entities to massive-scale, dynamic data, varying both in spatial and time dimension [11]. To address this development, many researchers have proclaimed the work with multivariate data sets to be an important task for future visualization research that will require significant advances in developing visualization algorithms. Raphael Fuchs et al. gave us an overview of typical techniques from various disciplines dealing with the complex multi-dimensional scalar, vector, and tensor data sets [12]. Hesselink et al. indicated four goals for future visualization research [13]: feature-based representation of data, compromising reduced visual complexity, increased information content and a visualization that matches the concepts of the application area. These goals are still available today. As pointed out by Google's Eric Schmidt, we are creating as much information every two days as we did from the dawn of civilization up until 2003 [14]. The situation we face shifts from the lack of data to the "big data" world. How to extract and visualize knowledge from massive spatiotemporal data effectively poses a great challenge [15].

Furthermore, the analysis and extraction of the raw data are more beneficial to researchers than the capture and visualization of raw data itself. Exemplified in a scenario, climate scientists may have a hypothesis about the atmospheric events from the visualization of climate data and would like to test and verify these assumptions. Knowledge-driven visualization systems meet that requirement and help the scientist to view information, discover knowledge, make a decision and plan for the future. In other words, these systems enable researchers to focus on regions of interest and to detect activity from massive spatiotemporal data over thousands of time steps. In this paper, we leave out a vast amount of work on knowledge extraction by identifying a cyclone from the spatiotemporal climate data, tracking the cyclone and verifying the cyclone trajectory with the dynamic simulation of cyclone characteristics.

The remainder of this paper is organized as follows. In Section 2, we summarize the previous work on the most important process of the knowledge-driven system—the cyclone identification algorithm and cyclone simulation approach. We then discuss the methodology of cyclone identification in Section 3. In Section 4, we briefly discuss the realization of wind simulation with graphics cards and the integration of identification results with a cyclone simulation for result validation. Section 5 is dedicated to introducing the data we use and analyzing the experimental results, including performance and accuracy. In the last chapter, we conclude the paper with a discussion of our method and the future research of the knowledge-driven visualization system.

## 2. Related Works

Web-based 3D (three-dimensional) geo-applications have been studied in various research projects using different technology, such as VRML (Virtual Reality Modeling Language), X3D (Extensible 3D) [16] and WebGL [17]. However, the 4D (four-dimensional) representation of time-varying phenomena in geo-visualization tools has not yet been thoroughly studied [18]. Resch identified a number of open research questions including mapping graphic variables to thematic expressivity, representation of the time dimension in 4D geo-applications and implementing a prototypical system to visualize marine spatial data [18]. Kang reported an empirical study that tested the usefulness of Web-based 4D construction visualization in collaborative construction planning and scheduling [19]. However, those research projects focus on the 4D representation of the atmospheric phenomenon rather than knowledge extraction from the raw data sets.

Usually, atmospheric phenomenon identification and tracking are more valuable to climate scientists than data visualization. In the field of atmospheric activity identification, Ozer et al.

introduced a prototype of activity detection in scientific visualization [20]. Their goal was to develop a framework and facilitate scientists to model and identify a spatiotemporal pattern from massive data sets. However, current estimates of cyclone variability and cyclone identification methods are usually derived from analyses of surface level pressure (SLP) fields (e.g., the NCEP/NCAR Reanalysis Project) [21]. These works assimilate observational data into a physical model to produce atmospheric fields. The accuracy of these analyses is severely limited over the oceans. In other research, remote measurements that cover the globe to detect cyclones are used to solve this issue. Scientists attempted to find out suitable features for cyclone identification by gathering statistics from remote sensing data. These data include aerial reconnaissance aircraft data, local radar data and the global scale quickSCAT satellite data. Ho et al. (2008) used the SVM (Support Vector Machine) classifier to identify the cyclone by considering the factor of wind speed, the wind direction, and the direction-to-speed ratio [22]. It is a feasible approach; however, the robustness of the classifiers should be refined. Much more research is focused on tropical cyclone identification where the characteristics of cyclones are more apparent and noticeable. Nguyen et al. (2014) gave a detailed introduction and evaluation of the tropical cyclone identification methods based on numerical models [23]. However, polar cyclones we are interested in are smaller and harder to recognize than tropical cyclones. This means some methods for tropical identification may not work in polar cyclone identification.

In the field of computational fluid dynamics (CFD), research focuses on identifying fluid vortices. Many classical algorithms have been proposed to identify vortices. The intuitive definitions depict a vortex in terms of closed or spiral streamlines, local pressure minima, and maximum vorticity contours. Holmen (2012) classified these vortex identification methods into four groups [24]. Figure 1 demonstrates the detailed classification of the four groups. Some representative algorithms are listed in the group.

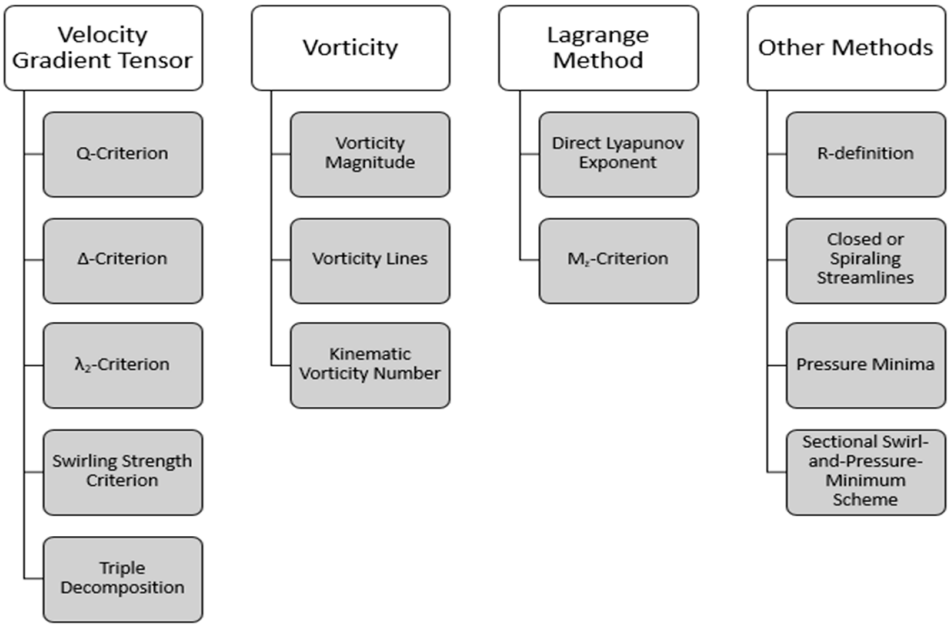


**Figure 1.** A classification of the traditional vortex identification method in the field of computational fluid dynamics.

Vorticity is deemed as one of the most natural choices for cyclone identification criteria since it indicates the physical characteristics of a vortex. However, it has been stressed that the vorticity criterion is limited to cyclone identification due to its failure to distinguish between pure shearing motion and the actual swirling motion. Important criteria have been proposed by analyzing the velocity gradient tensor. Vortex identification algorithms based on the velocity gradient tensor gradually turned

into the most widely used local method. However, it is difficult to differentiate cyclones with small vorticity in small shearing flow against cyclones with large vorticity in large shearing flow using the point-wise algorithm based on the velocity gradient tensor. The integration of particle trajectory is necessary within the Lagrange method which makes it computationally expensive. Meanwhile, other methods such as closed or spiral streamline and pressure minima are limited to the specific situation.

In our work, a combination method exploiting the pressure level and velocity is proposed for cyclone identification in order to reduce the limitation of the existing methods. Firstly, the pressure minima criterion is used to filter out noises and generate a potential cyclone eye set. An extra check with velocity direction and triple decomposition follow to identify the actual cyclone eye.

## 3. Methodology

In our work, a user-friendly knowledge-driven visualization system is our goal to facilitate climate analysis. The architecture of the system is demonstrated in Figure 2. The cyclone identification submodule, which is the most significant submodule in the system, enables users to filter and extract an atmospheric phenomenon from massive climate data. Rather than by drawing a geometric point on a digital earth as a representation for a cyclone, the wind simulation submodule provides a more vivid approach to validate the identification output.

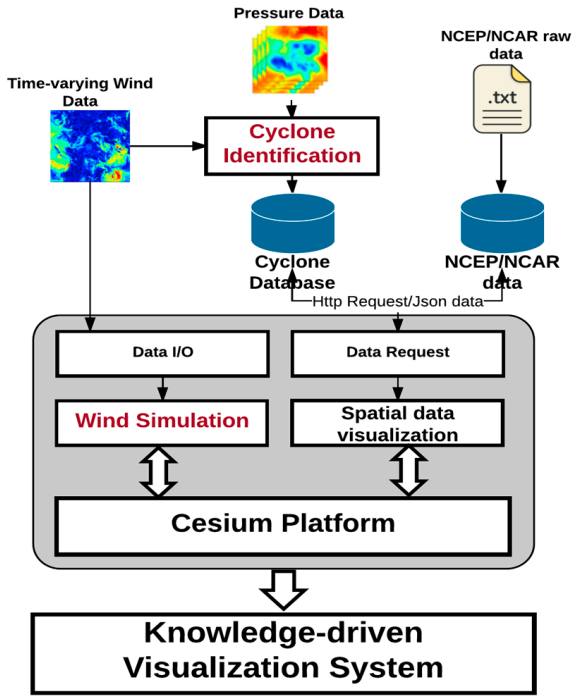


**Figure 2.** The system architecture of the web-based knowledge-driven visualization system.

Generally, in knowledge-driven visualization systems, scientists may prefer to discover the atmospheric activity at the North Pole instead of viewing the geometric information. More interest is targeted at the questions "When and where does the activity happen?" and "How long does that activity last?" Polar cyclones, which are a kind of that atmospheric activity, are climatological features that hover near the poles year-round [25]. The formation of polar cyclones is primarily influenced by the movement of wind and the transfer of heat in the polar region. Hence, more attention will be paid to the methodology of the identification of cyclones from massive time-varying wind field data and tracing the cyclone path. We subsequently leave out a few descriptions on the integration of the extracted cyclone with the wind visualization system.

A polar cyclone is always identified within a low-pressure zone embedded in a large mass of very cold air that lies atop the poles. Since a polar cyclone exists from the stratosphere downward into the mid-troposphere, a variety of pressure levels can be used for polar cyclone identification [26,27]. However, each cyclone eye has an extremely minimum pressure in its neighborhood, not vice versa. Hence, augmented techniques are necessary for filtering the potential cyclone eye. Given that we have the pressure data and wind velocity field, a combination of minimum pressure extraction and wind direction filter is used for cyclone identification in our method. Figure 3 illustrates the flow of our cyclone identification algorithm. First, we extract the minimum pressure in the neighborhood to find the potential cyclone eye. Second, wind field is used to filter out the actual cyclone eye. In our work, a combination of wind direction detection and triple decomposition are exploited to accomplish this goal.

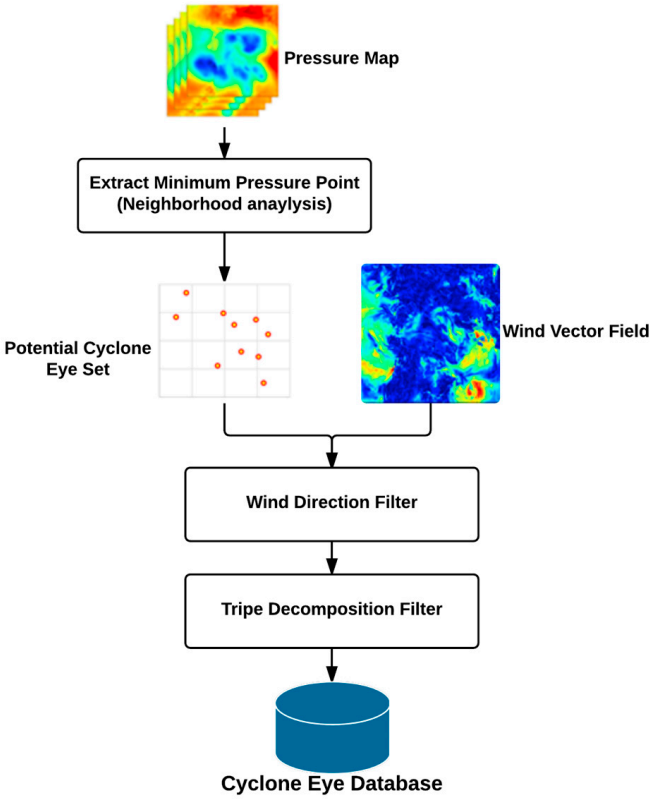


**Figure 3.** The workflow of our cyclone identification algorithm.

- Minimum pressure extraction

The depression in the pressure map characterized by the minimal pressure value could be identified effectively by performing a neighborhood operation in the spatial analysis [28]. The threshold range of neighborhood $r$ should be specified to generate the neighborhood area. Each pixel's value in the pressure grid is updated with the minimum value in its neighborhood; then a new pressure map is generated. The potential cyclone eye is identified where the pressure value in the original map and the new map are equal. Figure 4 gives an illustration of this process with $r$ specified as 5. In our experiments, the neighborhood operation is conducted using GRASS GIS (Geographic Resources Analysis Support System, geographic information system), a free and open-source GIS software suite in Python and the neighborhood range $r = 13$. Even though $r$ is an empirical value, it has a small influence on the outcome due to the spatial distance of two cyclones. After the minimal pressure value filter, a potential cyclone eye set is generated for further filtering purposes.

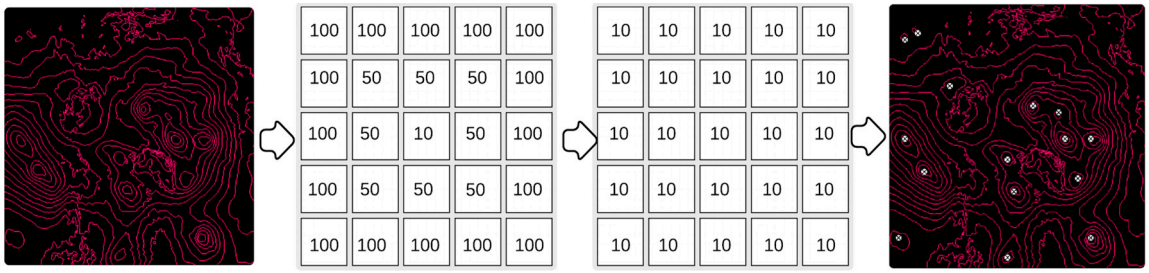


**Figure 4.** The process of potential cyclone eye identification using neighborhood analysis ($r$ = 5).

- Potential cyclone eye filter

It appears that the wind direction in the neighborhood of a cyclone eye composes a rotation circle from the physical characteristics. So the noise in the potential cyclone eye set might be filtered out by checking the change pattern of the wind direction within the local neighborhood of a cyclone eye. Four potential scenarios might be found near the potential cyclone eye in the northern hemisphere (seen in Figure 5). Scenario (a) has the most possibility to be found near the cyclone eye. To filter through these scenarios, a signum operation is carried out on the matrices containing the velocity components in relevant directions. For a potential cyclone eye, its four neighbors—up, down, left and right—are selected for direction filtering.

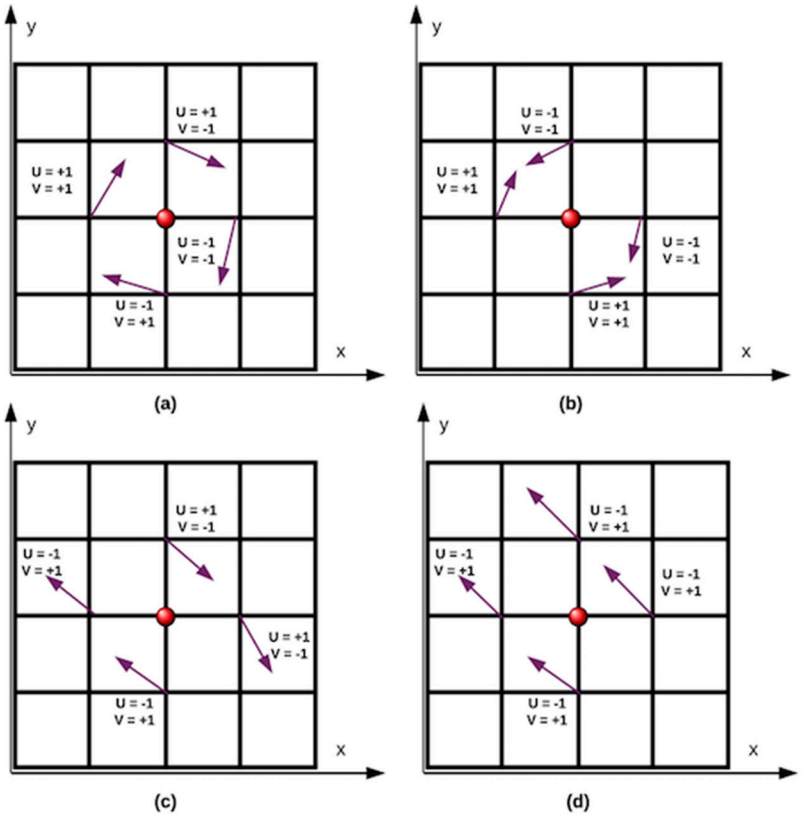


**Figure 5.** Four potential scenarios might be found near the potential cyclone eye in the Northern Hemisphere: (**a**) rotation wind; (**b**) strain wind; (**c**) shearing wind; (**d**) same direction wind.

In each scenario, Y components of velocity are considered with the left and right neighbor; X components with the up and down neighbor. Seen in Equation (1), $\boldsymbol{U}$ and $\boldsymbol{V}$ indicate the X component of the velocity and the Y component of the velocity, respectively. If the sum of the signum value of

the velocity matrix in the relevant direction equals 0, the direction might compose a rotation. With this principle, we can filter out the wind scenario in Figure 5d where the wind direction goes in the same direction.

$$\mathrm{Sgn}\left(v_{left}\right) + \mathrm{Sgn}\left(v_{right}\right) + \mathrm{Sgn}\left(u_{up}\right) + \mathrm{Sgn}\left(u_{down}\right) = 0 \quad (1)$$

$$\mathrm{Sgn}\left(v_{left}\right) + \mathrm{Sgn}\left(u_{up}\right) \neq 0 \quad (2)$$

An extra check is conducted to make sure the direction entails a rotation, as there are still three scenarios where the sum of the signum value equals 0. These scenarios are depicted in Figure 5a–c. To filter out the scenario in Figure 5b, another check illustrated in Equation (2) is done by checking the sum of the signum values for the left and upper neighbors. However, the scenario in Figure 5c cannot be filtered out by Equations (1) and (2). This indicates that the velocity data alone cannot distinguish pure shearing motions from the actual swirling motion of a cyclone.

To solve this issue, Kolar introduced a method regarding the triple decomposition of the velocity gradient tensor, which distinguishes the pure shearing motion and actual swirling motion by decomposing the velocity gradient tensor [29]. The aim is to decompose an arbitrary instantaneous state of the relative motion into three elementary motions. An illustration can be found in Figure 6.

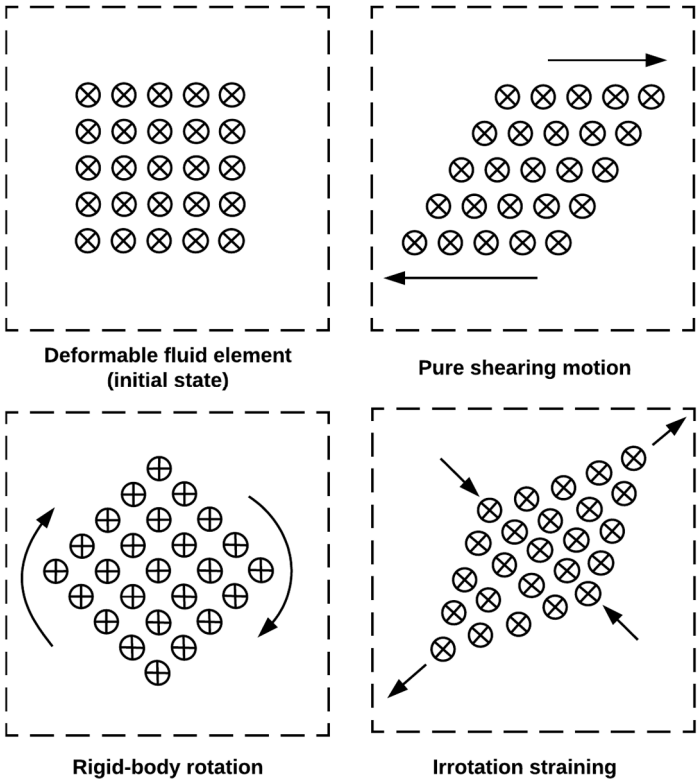


**Figure 6.** A qualitative model of three elementary motions of a flow [29].

The velocity gradient tensor will be decomposed into three components to represent three elementary motions where the pure shearing should be purely asymmetric, the rigid-body rotation should be antisymmetric and the irrotational staining should be symmetric. The decomposition strategy is based on the characteristic of the motion and the matrix is decomposed into three parts. Equations (3)–(6) illustrate the process [29]. The rigid-body rotation and irrotational straining are combined as the residential tensor.

$$\nabla u = \begin{bmatrix} u_x & u_y \\ v_x & v_y \end{bmatrix} = (\nabla u)_{re} + (\nabla u)_{sh} = (\nabla u)_{st} + (\nabla u)_{ro} + (\nabla u)_{sh} \quad (3)$$

$$(\nabla u)_{re} = (\nabla u)_{st} + (\nabla u)_{ro} = \begin{bmatrix} u_x & sgn(u_y)MIN\left(|u_y|, |v_x|\right) \\ sgn(v_x)MIN\left(|u_y|, |v_x|\right) & v_y \end{bmatrix} \quad (4)$$

$$(\nabla u)_{st} = \frac{\left((\nabla u)_{re} + (\nabla \mathrm{u})_{re}^{T}\right)}{2} \quad (5)$$

$$(\nabla u)_{ro} = \frac{\left((\nabla u)_{re} - (\nabla \mathrm{u})_{re}^{T}\right)}{2} \quad (6)$$

The cyclone eye regions are characterized by the non-zero rotation tensor and

$$|(\nabla u)_{st}| < |(\nabla u)_{ro}|$$

The identification output (the cyclone position in the grid index) will be stored in the cyclone database with PostGIS and used for the significant input of cyclone tracking. However, it still needs to be validated and estimated in the knowledge-driven system by comparing it with dynamic cyclone simulation and reanalysis data. Next, we give a brief introduction of the integration of identification output with real-time cyclone simulation.

## 4. Integrating Identification Output with Wind Simulation

Real-time wind simulation is the most intuitive and effective way to view cyclone activity. Like point clouds representing the surface of a 3D entity, large quantities of dynamic particles express physical phenomena effectively. By rendering massive unevenly distributed and animated particles, dynamic cyclone activities will be simulated and tracked from birth to death with the wind simulation submodule. Meanwhile, users can easily capture the dynamic cyclone by its appearance. Actually, the particle system has been widely used in experimental flow analysis. The integration of identification outcome with cyclone simulation enables us not only to validate the outcome but also to label the cyclone with a specific trajectory in the system. At this point, it is necessary to simulate the spatiotemporal wind field based on particle tracking in the web environment.

Particle tracing—which provides a Lagrange description of a problem by solving ordinary differential equations using Newton's law of motion—provides an effective approach for field visualization. A geometric entity or phenomenon is represented by thousands of discrete and animated particles. The integration process in each rendering frame is briefly introduced below. The particle position is calculated and updated in each frame with the integral Equation (7).

$$\boldsymbol{p}(t + t) = \boldsymbol{p}(t) + \int_{t}^{t+t} \boldsymbol{v}\left(\boldsymbol{p}(t), t\right) dt \quad (7)$$

$\boldsymbol{p}$ (t) and $\boldsymbol{p}$ (t + Δt) represent the particle position in time t and time t + Δt. Further, $\boldsymbol{v}\left(\boldsymbol{p}(t), t\right)$ indicates the velocity and is determined by position and time. The 4D wind field data is compressed into a video using VP9 to solve the issue of data transmission from the remote server on web environment.

Resch et al. evaluate five different technologies on many criteria, such as web browser support, implementation complexity, and performance [18]. WebGL is the best choice for us to visualize the wind data due to its characteristic of cross-platform and GPU (graphics processing unit) computing, enabling it to accelerate visualization [30,31]. To tessellate the wind data in a unified geometric frame, Cesium—an open-source JavaScript library for world-class 3D globes based on WebGL—is used for earth visualization [32]. Figure 7 illustrates the process of one-frame rendering in our method. Three passes which are particle initialization, particle advection, and particle rendering are executed on the GPU in one-frame rendering.

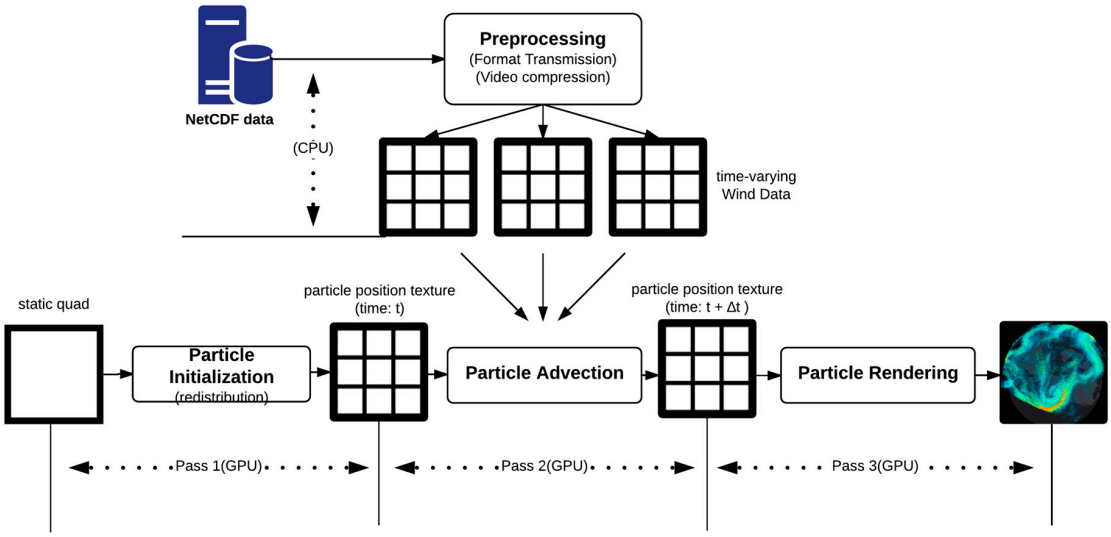


**Figure 7.** The workflow of particle-based wind data visualization. Three phrases of particle computing are executed on GPU.

Pass 1. Particle Initialization. Particle positions are initialized randomly and redistributed to emphasize the region of interest. The positions are stored in the RGB color components of a floating point texture along with particle lifetime in the alpha.

Pass 2. Particle Advection. The particle position is updated in each frame using the classical Euler scheme within the fragment shader in parallel. The wind vector from a random position used for moving the particle is accessed with the bi-linear interpolation on the GPU. A boundary test and death test need to be conducted to check if the particle should be recreated. Furthermore, a double frame buffer technique is used to avoid the write and read conflict. The output texture in particle advection is used for the input of particle rendering.

Pass 3. Particle Rendering. Once particle positions have been updated and fetched, the particles are rendered usually in the form of a texture billboard (pixel, oriented point spirits).

With the animation of particles, it is easy to visually distinguish and trace the vortex activity in the scenario (see cyclone A in Figure 8). The cyclone identification outcome is rendered in each frame along with the simulation. The cyclone position is queried from the spatial database with the property of time and the user-defined selective rectangle. The integration of the identification outcome with cyclone simulation helps to validate the accuracy of the identification method mentioned in Section 3. Meanwhile, it is a demonstration of how the cyclone extraction can be applied to real applications. The spatiotemporal query enables the user to focus on the interested cyclone within a specific time and space.

## 5. Analysis and Discussion

### *5.1. Data Introduction*

In our work, the 13 years (2000–2012) of sea level pressure (SLP) and wind velocity from the Arctic System Reanalysis (ASR) interim version are used for cyclone identification and wind simulation [33]. ASR-interim is a 30 km data set and is available through the NCAR Research Data Archive. There are 25 levels of data on the Z axis. Both the u-component and v-component winds are relative to a 360 × 360 grid. In the temporal dimension, the climate data were captured at three-hour intervals.

To validate the accuracy of our cyclone identification algorithm, the North Hemisphere Cyclone location from NCEP/NCAR Reanalysis data [34] is used as another comparison. This data set

comprises a 50-year record of daily extratropical cyclone statistics from 1958 to 2008. Cyclone locations were obtained by applying the updated Serreze's algorithm [21] to daily SLP data at six-hour intervals [35]. The parameters included in this data set are the position and central pressure of each cyclone, the distance the center of the cyclone traveled, whether the observation represents a cyclogenesis event, and the local Laplacian of the SLP and sea level pressure tendency at each cyclone eye. Due to the low resolution of the NCEP/NCAR data in the temporal dimension, the time interval for picking up the comparison data is set to six hours.

### *5.2. Experiment and Analysis*

The wind visualization demonstrations were run on a machine with a 2.7 GHz Intel Core i5 CPU and 16 GB of RAM. The graphics card was an AMD Radeon HD 6770 m with 512 MB of RAM. We exploited JavaScript to implement the particle rendering framework and GLslang (GLSL) shader to realize the core particle advection algorithm. The cyclone identification algorithm was implemented in Python and the NCEP/NCAR Reanalysis data was stored in a geometric database with PostGIS.

#### 5.2.1. Performance Analysis

Figure 8 depicts the screenshot of the 4D wind visualization. In this demonstration, the cyclone is easy to identify from the animated particles in an instantaneous frame (e.g., Cyclone A). Furthermore, by updating the wind field data through the time dimension, the cyclone's trajectory can be visually traced. Due to the particle redistribution, more particles distribute in the area with a large velocity magnitude which emphasizes the area with a cyclone. The simulation performance has a great influence on the user experience and the validation of the identification outcome. To address a realistic simulation, the particle number can optionally be edited and updated. Here, four particle samplers with the numbers specified as 65,536 (256 × 256), 262,144 (512 × 512), 1,048,576 (1024 × 1024), 4,194,304 (2048 × 2048) are applied. The time expense of particle rendering (PRT), the time expense of particle advection (PAT) and the measured frame rate are estimated in Table 1.

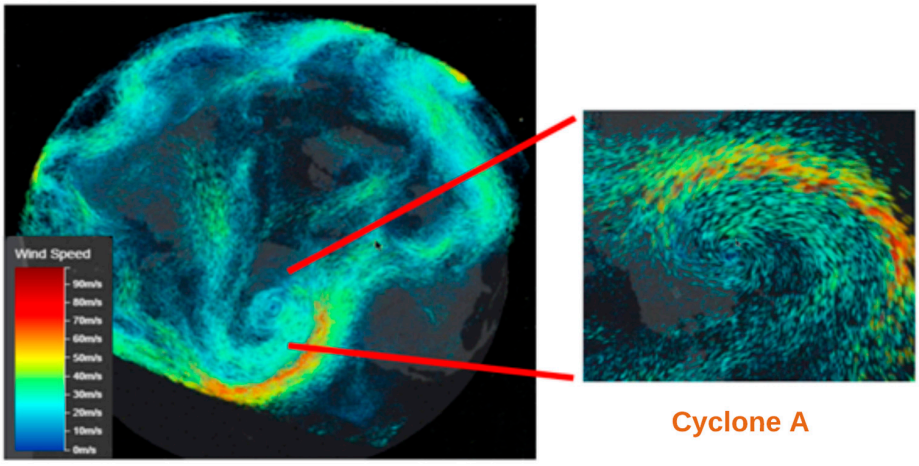


**Figure 8.** Screenshot of the wind field visualization (262,144 particles).

**Table 1.** Performance test (particle render time consumption, particle advection time consumption, frame rate) with different particle numbers.

| Particle Number | PRT | PAT on GPU | PAT on CPU | Frame Rate |
|---|---|---|---|---|
| 256 × 256 | 4 ms | 5 ms | 10 ms | 50.88 fps |
| 512 × 512 | 10 ms | 5 ms | 42 ms | 31.53 fps |
| 1024 × 1024 | 68 ms | 6 ms | 191 ms | 13.05 fps |
| 2048 × 2048 | 222 ms | 7 ms | 578 ms | 7.43 fps |

The particle rendering time (PRT) and particle advection time (PAT) rise with the increase of particle numbers, while the frame rate behaves inversely. In addition, the particle rendering time and particle advection time on the CPU maintain an exponential growth, while the particle advection time on the GPU is kept almost stable or increases slightly, as shown in Figure 9. We can conclude that exploiting the GPU for particle advection can effectively improve the performance.

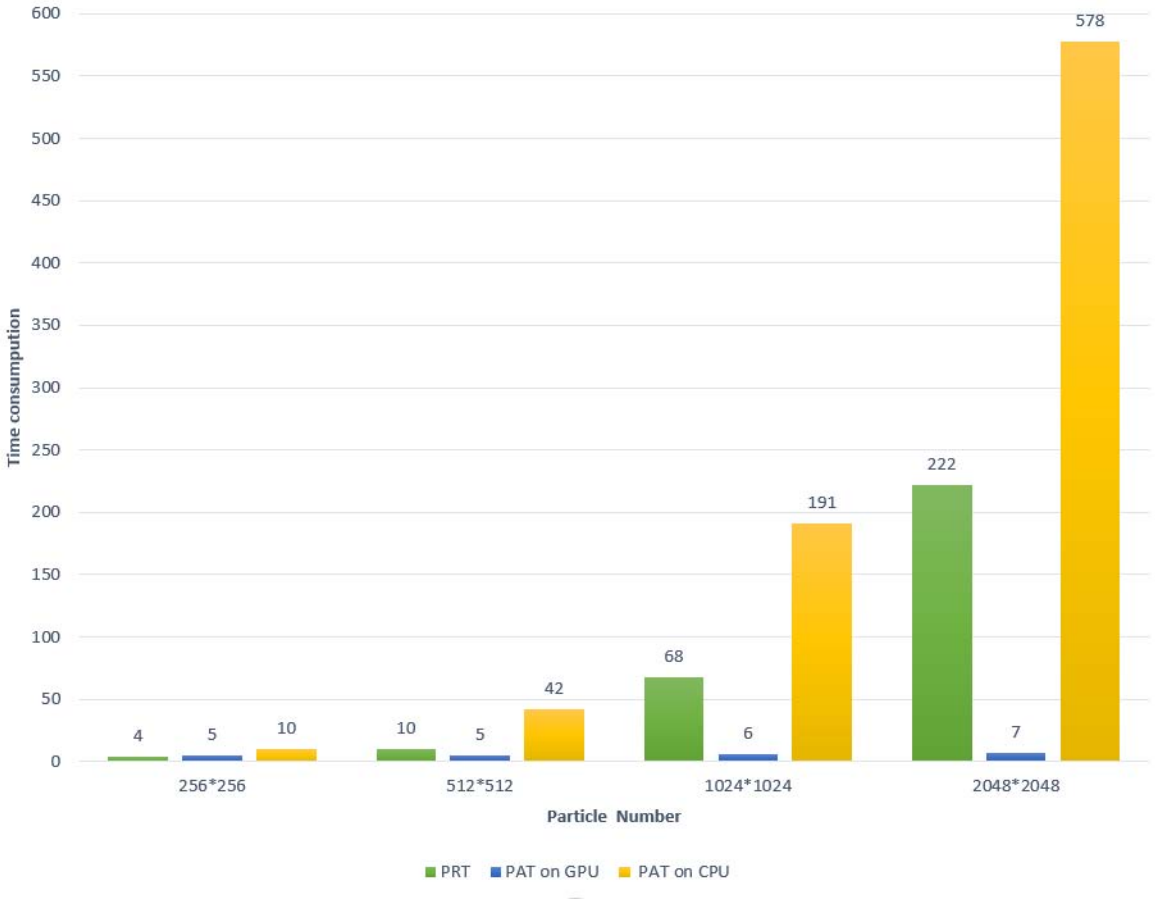


**Figure 9.** Time consumption of particle advection with different particle number.

### 5.2.2. Accuracy Analysis

The accuracy of the cyclone eye extraction algorithm is the most important factor to evaluate the algorithm. The accuracy estimation is conducted in two steps: comparison with figures generated by plotting the neighborhood of a potential cyclone eye and comparison with NCER/NCAR reanalysis data. After the potential cyclone eye set was captured, we plotted the wind direction in the neighborhood area of the potential cyclone eye with the streamplot function. A $6 \times 6$ neighbor grid of the potential point was specified in the experiment. With the output plot figure, it is easy to visually distinguish if the current potential candidate is a real cyclone eye or noise. In Figure 10, four potential cyclone eyes extracted with pressure data on 1 January 2007, 0:00 a.m., are taken as an example. Four plot figures are titled with the grid index coordinate of the potential cyclone eye. In addition, the four points are detected with the identification method proposed in Section 3. If the outcome indicates the point is a cyclone, the figure title is colored in red; otherwise, it is in green. For example, point (235,152) is identified as not a cyclone eye after detecting it with the proposed method, thus its title displays in green. However, the other three are cyclone eyes and their titles display in red. Hence, by comparing the color of the title and the wind characteristic in the corresponding plot figure, we can conclude that the outcomes of the proposed identification method match the real characteristics very well.

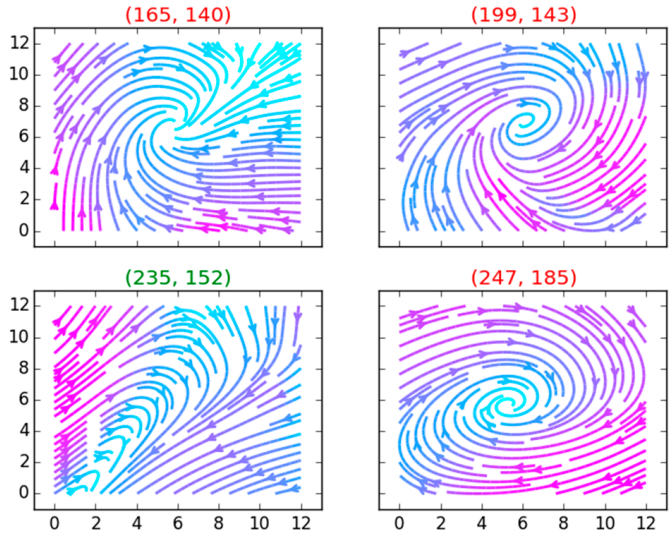


**Figure 10.** Comparison of the identification result with the plot figure (6 × 6 neighbor grid).

Given the complexity of the wind direction in the neighborhood of the potential cyclone eye, there is some noise in the identification outcome. The noise includes the points which are not cyclone eyes in the plotted figure but are identified as cyclone eyes by the proposed method and those which are cyclone eyes but are not identified as cyclones. Here, FBP (Number of potential cyclone eye) indicates the number of potential cyclone eye filters by pressure. MIS (wrong identification result) represents the noise in the result that is the sum of over-identification and miss-identification. The ACC (accuracy) of the identification method is calculated with Equation (8). To verify the algorithm, 182 potential cyclone eyes are extracted from eight groups of data captured in 2007. The identification statistical results are illustrated in Table 2. MIS 1 represents the noise of the outcome. The identification accuracy is over 90% and the average accuracy is 94.5%, which is displayed in row ACC 1.

$$\mathrm{ACC} = 1 - \frac{MIS}{FBP} \tag{8}$$

**Table 2.** Accuracy analysis results with eight groups of data in 2007. FBP is the element number in the potential cyclone eye set; MIS indicates the number of identification errors.

| ID | 20070100 | 20070106 | 20070112 | 20070118 | 20070200 | 20070206 | 20070212 | 20070218 | SUM |
|---|---|---|---|---|---|---|---|---|---|
| FBP | 26 | 19 | 21 | 20 | 23 | 25 | 26 | 22 | 182 |
| MIS 1 | 1 | 1 | 1 | 2 | 2 | 1 | 2 | 0 | 10 |
| ACC 1 | 0.9615 | 0.9473 | 0.9523 | 0.9 | 0.913 | 0.96 | 0.923 | 1.00 | 0.945 |
| MIS 2 | 1 | 1 | 0 | 1 | 1 | 2 | 1 | 1 | 8 |
| ACC 2 | 0.9615 | 0.9473 | 1.00 | 0.95 | 0.9565 | 0.92 | 0.9615 | 0.9545 | 0.956 |

To further estimate the identification accuracy, we compare the cyclone identification result with the cyclone location data from the NCEP/NCAR reanalysis data. Figure 11 depicts the visual comparison of the identification result and the NCEP data. The identification results are marked with red balloons while the NCEP/NCAR data is marked with yellow points. The two data sources match well in the figure. In addition, the output noise is estimated and labeled with MIS 2 in Table 2. The identification accuracy compared with the NCEP data is slightly higher than that with the plot figure. The average identification accuracy is 95.6%.

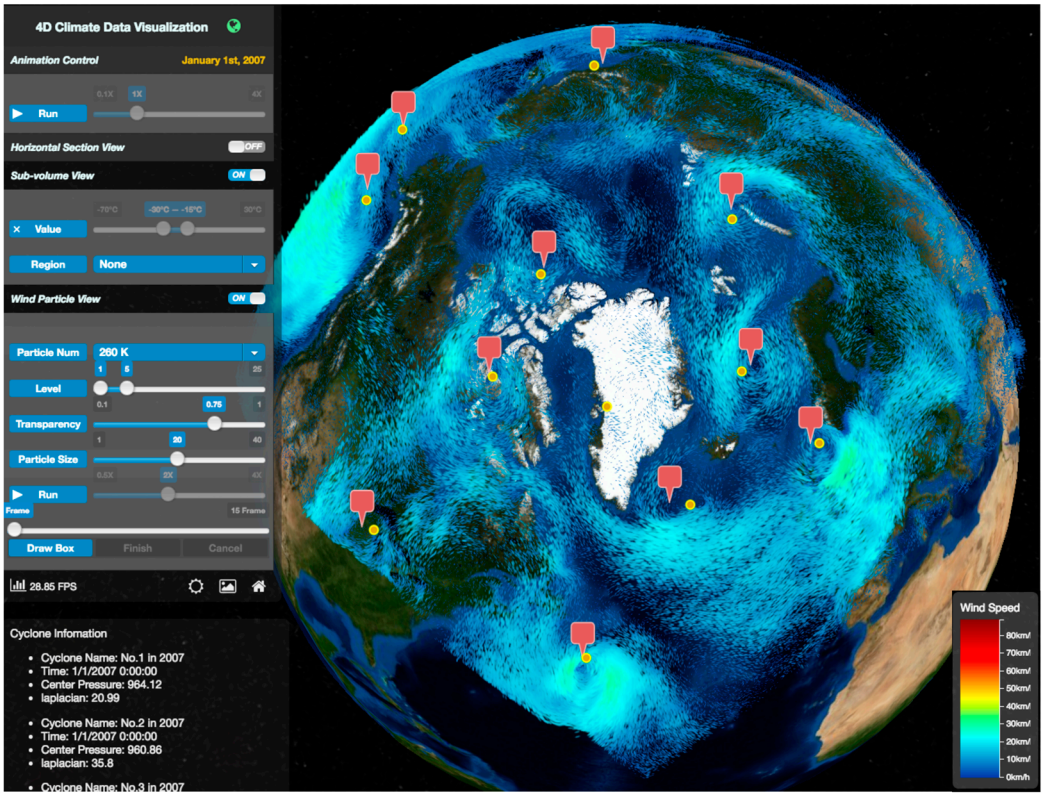


**Figure 11.** The comparison of the identification results with the NCEP/NCAR reanalysis data. Our identification output is marked with red balloons and the NCEP data is marked with yellow circle points.

## 6. Conclusions

Driven by helping scientists discover knowledge from raw atmospheric data around the North Pole, a cyclone identification approach is proposed to extract and track cyclones from spatiotemporal wind data in this paper. A combination of pressure minima criteria and velocity filter criteria is exploited to reduce the limitation of the existing criteria. The accuracy of the cyclone identification is demonstrated by comparing the identification result with the plotted figure and NCEP/NCAR reanalysis data using eight groups of data captured in 2007. The statistical results show that the proposed approach can effectively identify the complicated cyclones in the North Pole with an accuracy of over 95%. Based on this approach, a web-based knowledge-driven and decision-making system is architected where the 4D wind simulation is based on particle tracking.

Furthermore, by introducing the cyclone identification concept and method in the North Pole, this paper aims at facilitating atmospheric activity detection research on massive spatiotemporal climate data. The present framework should still be considered to be a work in progress and further work should be focused on real-time cyclone identification and performance optimization.

In the future, more work will be conducted on the automated activity detection technology and abstract identification method to extract variable atmospheric events. The detailed discussion should be taken over on the atmospheric phenomenon definition and universal detection scheme. Additionally, atmospheric event identification with Artificial Intelligence (AI) is another direction to be studied.

**Acknowledgments:** This project is supported by the National Science Foundation (PLR-1349259; BCS-1455349; and PLR-1504432).

**Author Contributions:** All authors contributed extensively to the work presented in this paper. Wenwen Li and Feng Wang conceived and designed the experiments. Sizhe Wang, Feng Wang and Wenwen Li developed the visualization platform for conducting the experiments. Feng Wang performed the experiments. Feng Wang, Wenwen Li and Sizhe Wang analyzed the data. Feng Wang and Wenwen Li wrote the paper. All authors discussed the results and implications and commented on the manuscript at all stages.

## References


1. Li, W.; Bhatia, V.; Cao, K. Intelligent polar cyberinfrastructure: Enabling semantic search in geospatial metadata catalogue to support polar data discovery. *Earth Sci. Inform.* **2015**, *8*, 111–123. [CrossRef]
2. Li, W.; Wu, S.; Song, M.; Zhou, X. A scalable cyberinfrastructure solution to support big data management and multivariate visualization of time-series sensor observation data. *Earth Sci. Inform.* **2016**. [CrossRef]
3. Li, W.; Wang, S.; Bhatia, V. PolarHub: A large-scale web crawling engine for OGC service discovery in cyberinfrastructure. *Comput. Environ. Urban Syst.* **2016**, *59*, 195–207. [CrossRef]
4. Li, W.; Shao, H.; Wang, S.; Zhou, X.; Wu, S. A2CI: A cloud-based, service-oriented geospatial cyberinfrastructure to support atmospheric research. *Cloud Comput. Ocean Atmos. Sci.* **2016**. [CrossRef]
5. Simmonds, I.; Burke, C.; Keay, K. Arctic climate change as manifest in cyclone behavior. *J. Clim.* **2008**, *21*, 5777–5796. [CrossRef]
6. McCabe, G.J.; Clark, M.P.; Serreze, M.C. Trends in northern hemisphere surface cyclone frequency and intensity. *J. Clim.* **2001**, *14*, 2763–2768. [CrossRef]
7. Bengtsson, L.; Semenov, V.A.; Johannessen, O.M. The early twentieth-century warming in the Arctic: A possible mechanism. *J. Clim.* **2004**, *17*, 4045–4057. [CrossRef]
8. Brümmer, B.; Thiemann, S.; Kirchgäbner, A. A cyclone statistics for the Arctic based on European Centre re-analysis data. *Meteorol. Atmos. Phys.* **2000**, *75*, 233–250. [CrossRef]
9. Cavalieri, D.J.; Parkinson, C.L.; Vinnikov, K.Y. 30-year satellite record reveals contrasting Arctic and AntArctic decadal sea ice variability. *Geophys. Res. Lett.* **2003**, *30*. [CrossRef]
10. Graversen, R.G. Do changes in the midlatitude circulation have any impact on the Arctic surface air temperature trend? *J. Clim.* **2006**, *19*, 5422–5438. [CrossRef]
11. Thomas, J.J.; Cook, A.K. A visual analytics agenda. *IEEE Comput. Graph. Appl.* **2006**, *26*, 10–13. [CrossRef] [PubMed]
12. Fuchs, R.; Hauser, H. Visualization of multi-variate scientific data. *Comput. Graph. Forum* **2009**, *28*, 1670–1690. [CrossRef]
13. Hesselink, L.; Post, F.H.; Van Wijk, J.J. Research issues in vector and tensor field visualization. *IEEE Comput. Graph. Appl.* **1994**, *14*, 76–79. [CrossRef]
14. Eric Schmidt: Every 2 Days We Create as Much Information as We Did Up to 2003. Available online: https://techcrunch.com/2010/08/04/schmidt-data/ (accessed on 20 April 2016).
15. Resch, B.; Hillen, F.; Reimer, A.; Spitzer, W. Towards 4D cartography—Four-dimensional dynamic maps for understanding spatio-temporal correlations in lightning events. *Cartogr. J.* **2013**, *50*, 266–275. [CrossRef]
16. Ming, W. A 3D web GIS system based on VRML and X3D. *IEEE Genet. Evol. Comput.* **2008**. [CrossRef]
17. Hering, N.; Rünz, M.; Sarnecki, L.; Priese, L. 3DCIS: A real-time browser-rendered 3d campus information system based on webgl. In Proceedings of the 2011 World Congress in Computer Science, Computer Engineering and Applied Computing, Las Vegas, NV, USA, 18–21 July 2011.
18. Resch, B.; Ralf, W.; Christoph, W. Web-based 4D visualization of marine geo-data using WebGL. *Cartogr. Geograph. Inf. Sci.* **2014**, *41*, 235–247. [CrossRef]
19. Kang, J.H.; Anderson, S.D.; Clayton, M.J. Empirical study on the merit of web-based 4D visualization in collaborative construction planning and scheduling. *J. Constr. Eng. Manag.* **2007**, *133*, 447–461. [CrossRef]
20. Ozer, S.; Silver, D.; Bemis, K.; Martin, P. Activity detection in scientific visualization. *IEEE Trans. Vis. Comput. Graph.* **2014**, *20*, 377–390. [CrossRef] [PubMed]
21. Serreze, M.C.; Carse, F.; Barry, R.G.; Rogers, J.C. Icelandic low cyclone activity: Climatological features, linkages with the NAO, and relationships with recent changes in the Northern Hemisphere circulation. *J. Clim.* **1994**, *10*, 453–464. [CrossRef]
22. Ho, S.S.; Talukder, A. Automated cyclone discovery and tracking using knowledge sharing in multiple heterogeneous satellite data. In Proceedings of the 14th ACM SIGKDD International Conference on Knowledge Discovery and Data Mining, Las Vegas, NV, USA, 24–27 August 2008.

23. Nguyen, L.T.; Molinari, J. Simulation of the downshear reformation of a tropical cyclone. *J. Atmos. Sci.* **2015**, *72*, 4529–4551. [CrossRef]
24. Holmén, V. Methods for Vortex Identification. Master's Theses, Lund University, Lund, Sweden, 21 November 2012.
25. Waugh, D.W.; Plumb, R.A.; Elkins, J.W.; Fahey, D.W.; Boering, K.A.; Dutton, G.S.; Volk, C.M.; Keim, E.; Gao, R.S.; Daube, B.C.; et al. Mixing of polar vortex air into middle latitudes as revealed by tracer-tracer scatterplots. *J. Geophys. Res. Atmos.* **1997**, *102*, 13119–13134. [CrossRef]
26. Schoeberl, M.R.; Hartmann, D.L. The dynamics of the stratospheric polar vortex and its relation to springtime ozone depletions. *Science* **1991**, *251*, 46–52. [CrossRef] [PubMed]
27. Cavallo, S.M.; Hakim, G.J. Composite structure of tropopause polar cyclones. *Mon. Weather Rev.* **2010**, *138*, 3840–3857. [CrossRef]
28. Podobnikar, T. Detecting mountain peaks and delineating their shapes using digital elevation models, remote sensing and geographic information systems using autometric methodological procedures. *Remote Sens.* **2012**, *4*, 784–809. [CrossRef]
29. Kolář, V. Vortex identification: New requirements and limitations. *Int. J. Heat Fluid Flow* **2007**, *28*, 638–652. [CrossRef]
30. Under the Hood: Using WebGL to Accelerate Advanced Physics Simulations in the Browser. Available online: https://concord.org/publications/newsletter/2012-fall/under-the-hood (accessed on 22 April 2016).
31. Bourges, S.M. *Graphics Programming on the Web WebCL Course Notes*; Motorola Mobility Inc.: Libertyville, IL, USA, 2013.
32. Keysers, J.H. *Review of Digital Globes 2015*; CRCSI: Victoria, Australia, 2015.
33. Arctic System Reanalysis (ASR) Project. Available online: http://dx.doi.org/10.5065/D6K072B5 (accessed on 15 November 2015).
34. Northern Hemisphere Cyclone Locations and Characteristics from NCEP/NCAR Reanalysis data. Available online: http://nsidc.org/data/nsidc-0423 (accessed on 2 January 2016).
35. Serreze, M.C.; Barrett, A.P. The summer cyclone maximum over the central arctic ocean. *J. Clim.* **2008**, *21*, 1048–1065. [CrossRef]